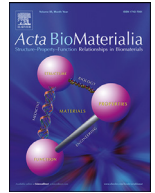




Contents lists available at ScienceDirect

Acta Biomaterialia

journal homepage: www.elsevier.com/locate/actbio

Full length article

A stochastic micro to macro mechanical model for the evolution of bone-implant interface stiffness

Jing Xie^{a,*}, Daniel Rittel^b, Keren Shemtov-Yona^{b,c}, Furqan A. Shah^d, Anders Palmquist^d^a State Key Laboratory of Explosion Science and Technology, Beijing Institute of Technology, 100081 Beijing, China^b Faculty of Mechanical Engineering, Technion - Israel Institute of Technology, 32000 Haifa, Israel^c The Maurice and Gabriela Goldschleger School of Dental Medicine, Department of Oral Biology, Tel Aviv University, 39040 Tel Aviv, Israel^d Department of Biomaterials, Sahlgrenska Academy, University of Gothenburg, Göteborg, Sweden

ARTICLE INFO

Article history:

Received 3 December 2020

Revised 5 June 2021

Accepted 9 June 2021

Available online xxx

Keywords:

Bone-implant interface

Stochastic modeling

Mechanical evolution

Percolation transition

ABSTRACT

Upon placement of an implant into living bone, an interface is formed through which various biochemical, biological, physical, and mechanical interactions take place. This interface evolves over time as the mechanical properties of peri-implant bone increase. Owing to the multifactorial nature of interfacial processes, it is challenging to devise a comprehensive model for predicting the mechanical behavior of the bone-implant interface. We propose a simple spatio-temporally evolving mechanical model – from an elementary unit cell comprising randomly oriented mineralized collagen fibrils having randomly assigned stiffness all the way up to a macroscopic bone-implant interface in a gap healing scenario. Each unit cell has an assigned Young's modulus value between 1.62 GPa and 25.73 GPa corresponding to minimum (i.e., 0) and maximum (i.e., 0.4) limits of mineral volume fraction, respectively, in the overlap region of the mineralized collagen fibril. Gap closure and subsequent stiffening are modeled to reflect the two main directions of peri-implant bone formation, i.e., contact osteogenesis and distance osteogenesis. The linear elastic stochastic finite element model reveals highly nonlinear temporal evolution of bone-implant interface stiffness, strongly dictated by the specific kinetics of contact osteogenesis and distance osteogenesis. The bone-implant interface possesses a small stiffness until gap closure, which subsequently evolves into a much higher stiffness, and this transition is reminiscent of a percolation transition whose threshold corresponds to gap closure. The model presented here, albeit preliminary, can be incorporated into future calculations of the bone-implant system where the interface is well-defined mechanically.

Statement of significance

A simple, physically informed model for the mechanical characteristics of the bone-implant interface is still missing. Here, we start by extending the reported mechanical characteristics of a one cubic micrometre unit cell to a 250 μm long interface made of 1 μm thick layers. The stiffness of each cell (based on mineral content) is assigned randomly to mimic bone micro-heterogeneity. The numerical study of this interface representative structure allows for the simultaneous determination of the spatio-temporal evolution of the mechanical response at local (discrete element) and global (overall model) scales. The proposed model is the first of this kind that can easily be incorporated into realistic future models of bone-implant interaction with emphasis on implant stability and different loading conditions.

© 2021 Acta Materialia Inc. Published by Elsevier Ltd. All rights reserved.

1. Introduction

Since the discovery in the 1960s, osseointegration has revolutionized the fields of medicine and dentistry, with very high

long-term clinical survival of metal implants intended for permanent anchorage in bone [1,2]. Several definitions exist for the term osseointegration, of which most are based on the inter-relations between the living bone and the load-bearing implant [3]. These inter-relations rely on the biomechanical integrity of the bone-implant interface and/or the contact quality between bone tissue and the implant material.

* Corresponding author.

E-mail address: jxie@bit.edu.cn (J. Xie).

Peri-implant healing is a dynamic process. This healing process involves an immune response, angiogenesis, osteoprogenitor cell recruitment, bone formation, and bone remodeling [3,4]. The control of healing is multifactorial in nature (including implant material, surface chemistry/topography, status of the host bone, surgical parameters etc.) [5,6]. Bone formation occurs both from the osteotomy border (created during implant bed preparation) as well as from the implant surface [7]. These distinct processes are termed Distance Osteogenesis (DO) and Contact Osteogenesis (CO), respectively [8]. This process is accompanied by physical changes, during which the biomechanical properties of the bone-implant interface (e.g., the interfacial strength) are established [9]. Direct bone apposition to the relatively stable metal implant surface, that happens during this process, allows for effective load-transfer from the external prosthesis to the surrounding bone tissue, thereby enabling bone homeostasis and long-term function [4]. In other words, the bone-implant interface is the spatial part of the system through which all the chemical, biological and mechanical interactions take place.

Bone healing, in response to different variables (implant material, implant geometry, surface structure, loading conditions, surgical procedures and healing time points), can be assessed experimentally using histology, molecular biology or analytic methods using microscopic techniques [6]. However, these experimental studies are largely dependent on the selected model and the sensitivity of the test methods and their limitations. For those reasons, experimental work is often combined with numerical modeling in a so-called hybrid experimental-numerical approach.

Two approaches are used: a homogenized macroscale model in which the bone structure is replaced with a solid equivalent one, and a high-resolution microscale model in which the minute microstructural details are included [10]. These two complementary approaches are usually applied to bone analysis without addressing specifically the interface. The classic homogenization procedure, based on the asymptotic or Representative Volume Element (RVE) method [11], has been used to analyze the bone structure for three decades. However, averaging the microscale structure and replacing it with a solid model with equivalent material properties leads to the loss of local structural information that is important for precise diagnosis and treatment. A recent review of bone modeling approached provides a substantial literature survey and profound discussion on this topic [12].

Simplified numerical models (finite element simulations) of the bone-implant complex usually assume a perfectly bonded state, which is basically unrealistic because the implant is never fully bonded. Contact analyses using different frictional coefficients have also been used to simulate different grades of integration during the osseointegration process [13–15]. Those showed some agreement with *ex vivo* measurements [16], but the relationship between the friction coefficient, bone quality, and the implant surface roughness is still lacking and unfortunately does not include the complex nature of the bone and its hierarchical structure. While some of these models take into account the bone-implant contact, i.e., the fraction of the implant surface directly abutting mineralized bone, which is a key determinant of implant stability [17], other parameters such as implant surface roughness (and the resulting interfacial interlocking) or the temporal evolution of stiffness of the bone-implant interface zone have not been considered.

The true nature of the bone-implant interface remains open to interpretation. The description considered here is that of a finite width zone within which various highly complex physicochemical interactions occur between the implant surface and the surrounding bone [4]. The ‘interface’ therefore encompasses the immediate bone-implant boundary together with a limited volume of peri-implant bone, which is approximately one implant radius, within

which strain fields originating from implant loading extend radially outwards [18].

In addition to water and non-collagenous proteins, the fundamental components of bone extracellular matrix, type-I collagen and mineral, form mineralized collagen fibrils (MCF) that arrange into fibrillar arrays [19]. The mineral phase of mammalian bone is exclusively ion substituted, carbonated apatite and no evidence of other calcium phosphates (e.g., beta tricalcium phosphate) has yet been reported [20]. Apart from extrafibrillar mineral that resides between adjacent collagen fibrils, each individual collagen fibril is composed of alternating gap regions and overlap regions [21] that contain mineral. Increase in mineral content of a single MCF leads to an increase in the Young’s modulus, strength, and toughness [22]. But although, the strength and toughness of bone are related to its composition and organization on the nanometer scale [23], the mutual interaction between a dental implant and the surrounding alveolar bone is a multiscale problem [13,24]. Micromechanical models, of the above-mentioned nature, while providing precious information at the microscale, have not been yet extended to the macroscopic scale, using e.g., statistical modeling assumptions.

In addition to being inherently multiscale in design, the bone-implant interface is heterogeneous in organization. Such heterogeneity can be taken into account by means of a stochastic assignment of the Young’s modulus to the elementary MCF unit cell. The immediate boundary at the bone-implant junction is made up of mineralized collagen fibrils, both in human [25,26] and animal models [27]. In the vicinity of the implant surface, mineralized collagen fibrils are co-aligned with the implant surface [28], which may be explained by the manner in which bone forming cells (i.e., osteoblasts) attach on to the implant surface and terminally differentiate into osteocytes [29,30]. At larger distances (e.g., beyond ~40 μm) from the implant surface, however, bone forming cells may be less sensitive to the implant surface contour, and the co-alignment is gradually lost [28,31].

It is apparent that a simple, yet physically informed model spanning multiple length scales, from micro- to the macroscopic scale, of the kind that could easily be implemented in numerical studies of the bone-implant interaction, is still missing. To this end, we describe a systematic modeling approach aimed at elucidating the mechanical properties of the bone-implant interface and the temporal evolution thereof. Starting at the level of the MCF unit cell, the concept is extended to the structural interfacial scale by means of statistical assignment of the mechanical stiffness of each cell. The model predicts the macroscopic interfacial stiffness and its temporal evolution as a function of mechanical and topological changes related to peri-implant osteogenesis. This simplified, yet physically realistic mechanical model of the bone-implant interface, can be successfully implemented in future numerical models aimed at investigating the interaction of the bone with the implant under various realistic loading scenarios.

2. Materials and methods

2.1. The evolving bone-implant interface model

The dimensions of the cuboid bone-implant interface model are set to $50 \times 50 \times 250 \mu\text{m}^3$, divided into three distinct evolving regions: CO region, gap zone (unmineralized region) and DO region. The length of each zone evolves gradually as a result of the progression of CO and DO regions and subsequent shrinkage (and closure) of the gap region. The model, as illustrated (Fig. 1a), is based on the following three main assumptions, noting that we use the terms *unit cell* and *finite element*, both having identical meaning and being unrelated to a biological cell.

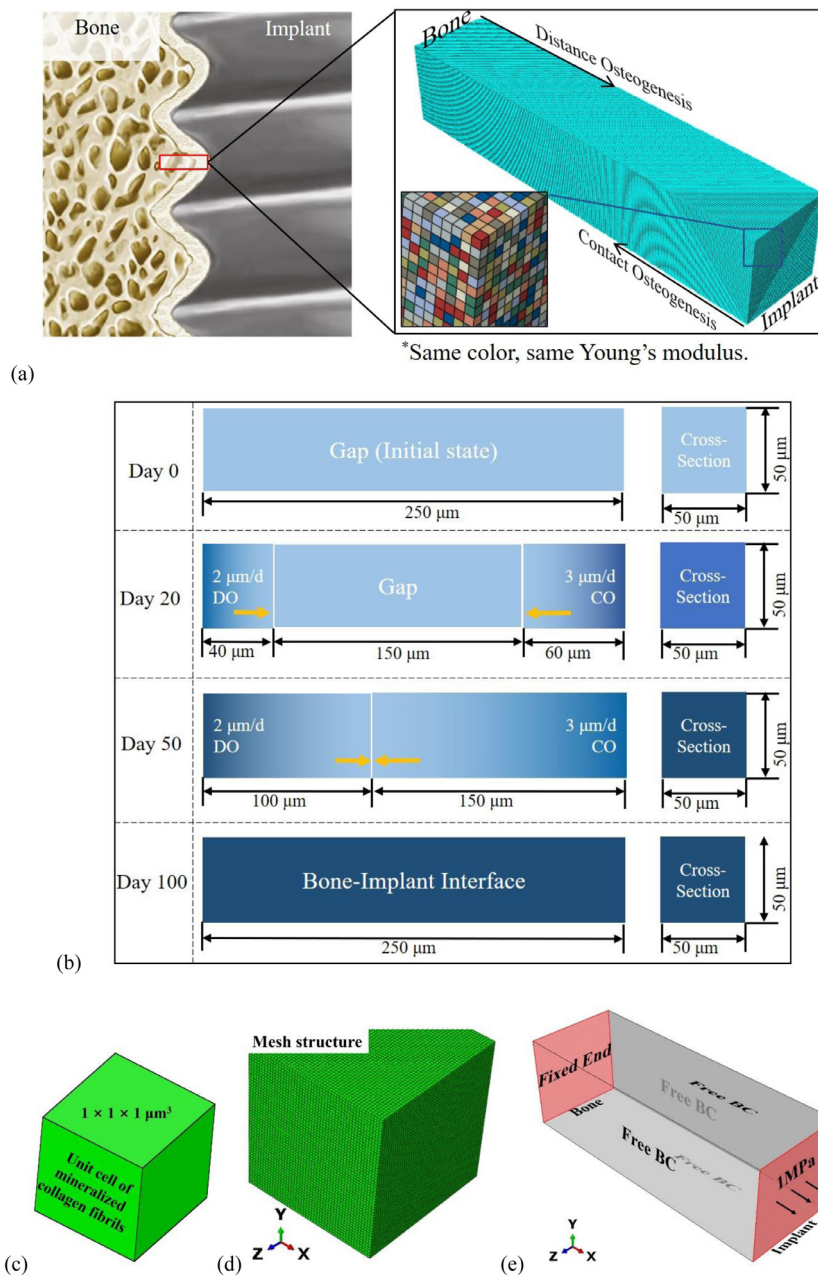


Fig. 1. (a) Schematic representation of the finite element bone-implant interface model. (b) Schematic representation of the kinetics of peri-implant osteogenesis. (c) Unit cell of mineralized collagen fibrils. (d) Regular mesh structure. (e) Boundary conditions (BC) of the model.

- 1 The minimum and maximum Young's modulus values for the MCF unit cell are obtained from a sub-micron level model where MCFs have been idealized as straight cylinders (100 ± 5 nm in diameter), randomly oriented with a dispersion of $\pm 15^\circ$ with respect to the long axis of the cylinder [32–34].
- 2 The kinetics of bone healing (Fig. 1b), are assumed for each direction of peri-implant osteogenesis, namely CO and DO [35]. CO extends away from the implant surface and progresses at a rate about 30% faster than DO, which progresses in the opposite direction (i.e., towards the implant surface), with rates set initially to 3 $\mu\text{m/day}$ and 2 $\mu\text{m/day}$, respectively [7]. Two additional scenarios were simulated where, at constant DO (2 $\mu\text{m/day}$), CO occurs either at the same rate as DO (2 $\mu\text{m/day}$) or slower than DO (1 $\mu\text{m/day}$).
- 3 The kinetics-coupled evolution of the bone-implant interface stiffening is assumed to start from the most compliant initial

state (at day 0) up to the stiffest state, in steps of 10 days, since the healing time for the implant takes up to about 6–12 weeks [36].

The length of the evolving bone-implant interface, 250 μm initially, is based on the depth of a typical screw-shaped M2 implant used in rats, which is then the longest span that CO and DO regions should collectively bridge. The cross-section of the evolving interface, $50 \times 50 \mu\text{m}^2$, is more arbitrary but approximated to the length scale at which osteoblasts connected by gap junctions as a cohort of cells (50–100 μm in diameter) [37]. At such distances, osteoblasts function together as a group and the extracellular matrix can be assumed to have all been deposited within a short span of time and therefore mineralized to a similar extent [38,39].

The unit cell (or mesh seed, the common technical name for the typical element size) was set to $1 \times 1 \times 1 \mu\text{m}^3$ (Fig. 1c), resulting in a total of 625,000 C3D8R elements in the model (Fig. 1d).

In another words, there are 250 layers between the two ends, and each layer has 2,500 (50×50) elements. Free boundary conditions are applied to the four side faces (Fig. 1e). One end (towards the native bone) is fully constrained, and the other end (towards the implant surface) is subjected to a constant 1 MPa tensile stress. Note that any other value could have been selected as long as the model remains linear elastic.

In the absence of reported measured Poisson's ratio for the MCF, the latter was arbitrarily set to 0.3 based on analytical calculations on MCF arrays [40]. The Poisson's ratio of 0.3 is well accepted since the sensitivity of this value is minimal [41] such that by varying it between 0.2 and 0.4, the E values for bone change only by ~8% [42].

All the simulations were solved using the commercial finite element program Abaqus (version 6.14, Simulia, Providence, RI) [43]. Multiple simulations were run in 10-day increments using 4 CPUs, and each case takes roughly 2,000 s CPU time. At constant DO (2 $\mu\text{m}/\text{day}$), varying CO (3 $\mu\text{m}/\text{day}$, 2 $\mu\text{m}/\text{day}$ and 1 $\mu\text{m}/\text{day}$) required between 11 and 17 simulations.

2.2. Determination of Young's modulus

Adapted local Young's modulus values were extracted from the MCF model of Wang and Ural [33], based on structural and compositional parameters. The computed Young's modulus, E_L , of the MCF unit cell is a function of the mineral volume fraction of the overlap region, ϕ_{ol} , that is $E_L = ae^{b \times \phi_{ol}} + c$ where a , b , and c are curve fitting coefficients. Considering different interactions between MCFs (i.e., cohesive behavior), the Young's modulus of the MCF unit cell along the longitudinal direction E_L ranges from 1.62 to 25.73 GPa. The detailed explanation follows.

The lowest E_L would appear for the unmineralized MCF ($\phi_{ol} = 0$) combined with a weak interaction between MCFs, according to:

$$E_L = -10.07e^{-20.05 \times \phi_{ol}} + 11.69 = -10.07e^{-20.05 \times 0} + 11.69 = 1.62 \text{ GPa} \quad (1)$$

The highest E_L would appear for the fully mineralized MCF ($\phi_{ol} = 0.4$) combined with a strong interaction between MCFs, such that:

$$E_L = -22.92e^{-12.05 \times \phi_{ol}} + 25.91 = -22.92e^{-12.05 \times 0.4} + 25.91 = 25.73 \text{ GPa} \quad (2)$$

Note here that the weak and strong interactions have different normal and shear strength values, respectively. In principle, the effective critical energy release rate (not accounted for in this work) is also different.

First, the reference modulus representing the maximum value of E increases linearly from 1.62 GPa at day 0 to 25.73 GPa at gap closure. Studies conducted by Ladd and Kinney [44] and by Cody et al. [45] indicate that discretization of bone architecture leads to around 20% of variance in the strength, the minimum and maximum values of modulus in the finite element model are thus bounded within a reasonable $\pm 20\%$ margin.

The assignment of E values is a two-step process. As the CO and DO regions extend towards each other, and the gap region shrinks (i.e., gap filling). At gap closure, CO and DO regions meet each other and there is no more unmineralized region. From thereon (stiffening of the closed gap), the modulus increases with time until it reaches the maximum, statistically uniform value at day 100 (Fig. 1b). To each of 2,500 elements in each layer, starting at the lowest range of values on day 0 (between 0.8×1.62 GPa and 1.2

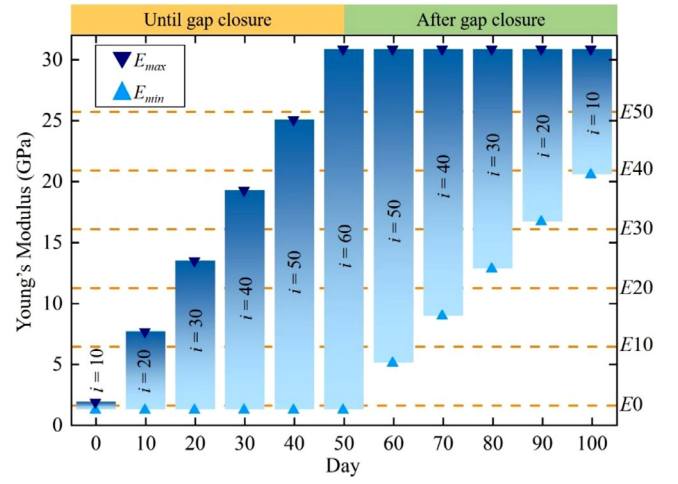


Fig. 2. The minimum-maximum range of Young's modulus of the bone-implant interface over a 100-day period for CO: 3 $\mu\text{m}/\text{day}$ and DO: 2 $\mu\text{m}/\text{day}$. Young's modulus values E0, E10, E20, E30, E40, and E50 represent the maximum values at days 0 (1.62 GPa), 10 (6.44 GPa), 20 (11.26 GPa), 30 (16.08 GPa), 40 (20.91 GPa), and 50 (25.73 GPa).

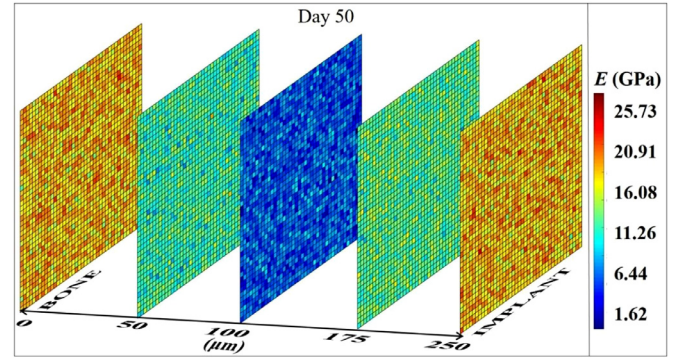


Fig. 3. Random material distribution for different layers of interface on day 50 at CO: 3 $\mu\text{m}/\text{day}$ and DO: 2 $\mu\text{m}/\text{day}$.

$\times 1.62$ GPa) and gradually increasing until gap closure where the range of moduli is maximal (between 0.8×1.62 GPa and 1.2×25.73 GPa) (Fig. 2). After gap closure, the maximum value is kept constant while the minimum value increases linearly with time to ultimately reach 0.8×25.73 GPa to mimic stiffening evolution.

Young's modulus profiles are assigned through a process of randomization. The range of E values is subdivided into i classes. Beginning with 10 classes on day 0 for the first interval of E , 10 more classes are added for every successive 10-day period until gap closure. Beyond gap closure, accounting for decreasing range of E values, there is a decrease by 10 classes of E values for every successive 10-day period (Fig. 2). The idea behind the number of classes is to provide a satisfactory discretization of the range of E values.

The modulus assignment algorithm is explained further by the following example. In order to maintain full randomization, the elements of each layer are first reassigned numbers in the range of 1–2,500 to avoid contiguity of elements prior to assigning the E values. For each layer, the number of i classes depends on the kinetics of the healing process and varies with each day. The cross-section distribution of selected layers at day 50 is presented to exemplify the randomness of assigned E values (Fig. 3).

Therefore, the average E value (\bar{E}) varies each day between E_{\min} and E_{\max} , and can be expressed as:

$$\bar{E} = \sum_i a_i E_i \quad (3)$$

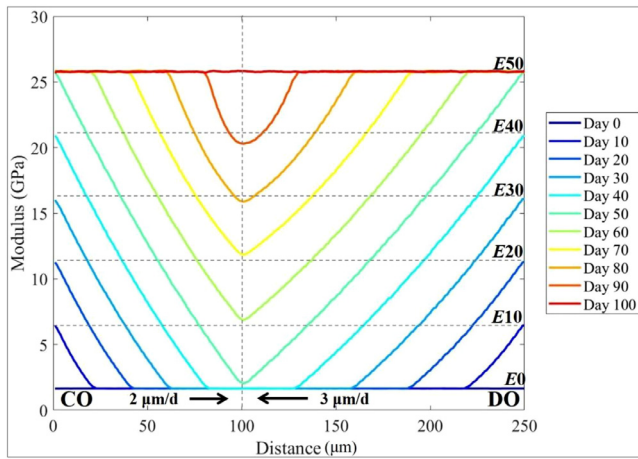


Fig. 4. Spatial evolution of the average Young's modulus along the bone-implant interface over a 100-day period at CO: 3 $\mu\text{m}/\text{day}$ and DO: 2 $\mu\text{m}/\text{day}$.

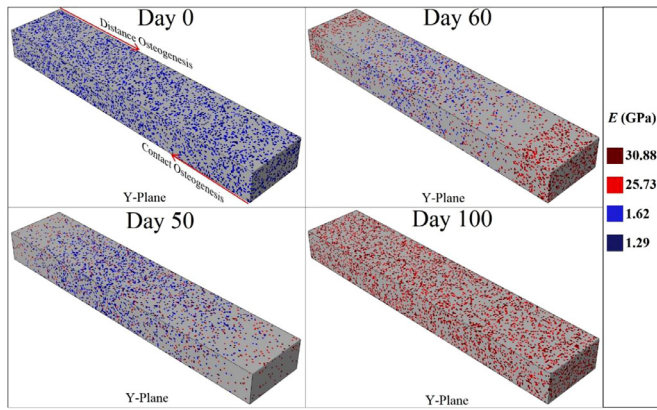


Fig. 5. Distribution of typical average modulus values over a 100-day period at CO: 3 $\mu\text{m}/\text{day}$ and DO: 2 $\mu\text{m}/\text{day}$. Only the upper and lower classes of E values for each respective time-point are displayed, and all the remaining classes of E values in between are represented in grey.

where a_i is a weighting coefficient for each of the i classes, obtained by dividing the number of elements within each i class by the total number of elements in each layer. The sum of all the weighting coefficients for each layer is always 1.

To allow for gradual stiffening, the weighting algorithm is propagated linearly such that with time, any given layer contains a higher proportion of higher E value elements. The average modulus of each 1 μm thick layer is therefore the arithmetic mean all the Young's modulus values within this layer. All layers are fully compliant at day 0. The first layers to increase in stiffness are those nearest to the implant surface in the case of CO and nearest to the native bone in the case of DO, sequentially followed by successive neighboring layers. By extension to both mutually opposite directions of peri-implant osteogenesis, i.e., CO and DO regions, and across the entire bone-implant interface model, a spatial gradient of average E values is achieved (Fig. 4).

An overall view of the randomness of the assigned modulus can be observed in Fig. 5 where compliant cells prevail at day 0, that gradually but not entirely, disappear by gap closure (i.e., day 50 at CO: 3 $\mu\text{m}/\text{day}$, DO: 2 $\mu\text{m}/\text{day}$) while being simultaneously replaced by stiffer cells.

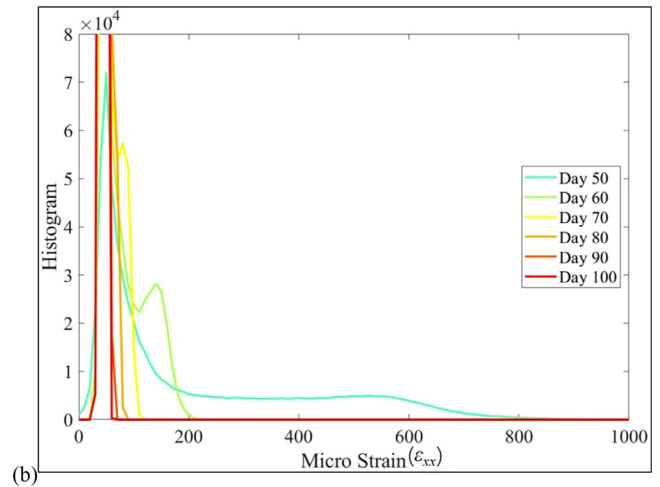
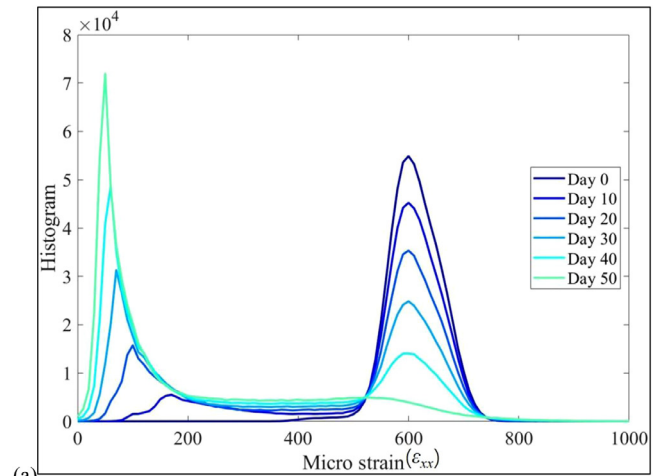


Fig. 6. Micro strain distribution over a 100-day period at CO: 3 $\mu\text{m}/\text{day}$ and DO: 2 $\mu\text{m}/\text{day}$. (a) Gap closure; from day 0 to day 50. (b) Stiffening; from day 50 to day 100.

3. Results

3.1. Evolution of strain distribution

The distribution of the longitudinal micro strain (ϵ_{xx}) varies over the 100-day period. The heterogeneity intensifies from day 0 to day 50 (Fig. 6a), then decreases gradually until day 100, where the distribution is quite narrow and is centered at $\sim 40 \mu\epsilon$ (Fig. 6b).

By comparing both phases, i.e., gap closure from day 0 to day 50 (Fig. 6a) and stiffening from day 50 to day 100 (Fig. 6b), the peak of micro strain can be seen to shift from higher values at day 0 (ϵ_{xx} : ~ 600) to lower values at day 100 (ϵ_{xx} : ~ 40), which is statistical evidence that the bone-implant interface undergoes a dynamic evolution from compliant to stiff. The valley between the two peaks (ϵ_{xx} : ~ 600 at day 0 and ϵ_{xx} : ~ 40 at day 50) may be explained by the discontinuous distribution of Young's modulus, attributable to the discretized classes of E values in the material model. More classes of Young's modulus will more precisely describe the deformation behavior of the interface.

3.2. Longitudinal strain

The longitudinal strain varies with time and evolves over the 100-day period (Fig. 7a). Since the material model is linearly elastic, the strain map does not disclose information that differs from the Von Mises stress map (not shown here). The material is

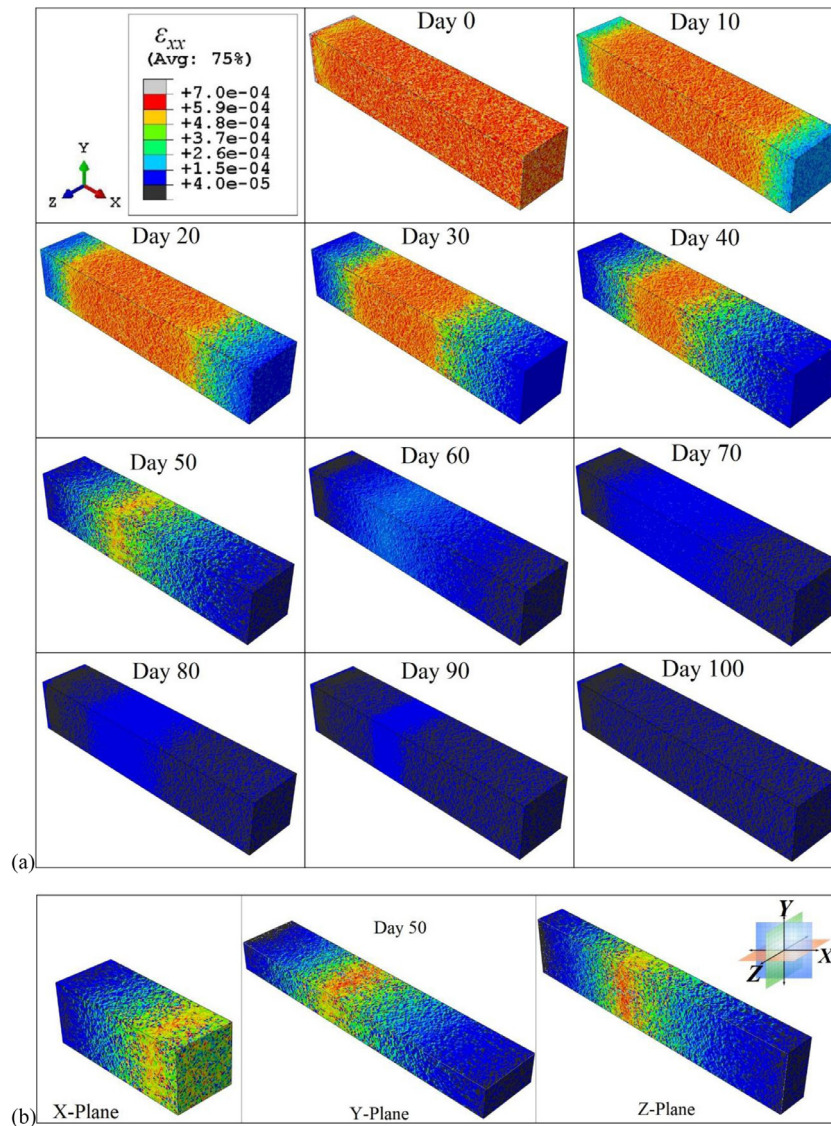


Fig. 7. (a) The evolution of X-axis strain distribution over a 100-day period at CO: 3 $\mu\text{m}/\text{day}$ and DO: 2 $\mu\text{m}/\text{day}$. As for the case of the stress, the strain tends towards more homogeneity as time elapses. (b) Three views of the longitudinal (X-axis) strain distribution on day 50.

isotropic, and the same degree of heterogeneity is evident in all three mutually perpendicular planes (Fig. 7b). The strain values are nevertheless of interest if bone remodeling, according to Wolff's law [46], is considered.

3.3. Evolution of resultant stiffness

Resultant stiffness (structural apparent stiffness) of the bone-implant interface structure (Fig. 8) is calculated by dividing the applied stress (boundary condition) by the macroscopic nominal strain resulting from the overall relative elongation of the entire model. This parameter represents the macroscopic mechanical response of the bone-implant interface as a structural element of the bone-implant system. A clear sigmoidal structure is obtained, such that up to the point of gap closure (e.g., day 50 at CO: 3 $\mu\text{m}/\text{day}$, DO: 2 $\mu\text{m}/\text{day}$), the resultant stiffness does not increase significantly, but after gap closure, the resultant stiffness increases significantly and gradually levels off by day 100. A clear distinction can be made between two states: open gap and closed gap.

In order to study further the influence of the kinetics of peri-implant osteogenesis, two additional cases were simulated: (i) CO (2 $\mu\text{m}/\text{day}$) occurring at the same rate as DO (2 $\mu\text{m}/\text{day}$), and (ii)

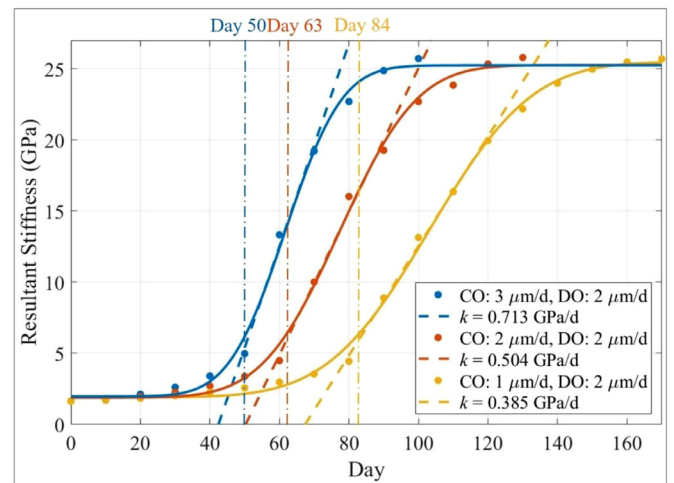


Fig. 8. The evolution of resultant stiffness at constant DO but varying CO. Solid lines are polynomial fitting curves. Broken lines represent the slope of upward phase. Vertical dash-dotted lines indicate the time of gap closure for the respective CO values.

CO (1 $\mu\text{m/day}$) occurring slower than DO (2 $\mu\text{m/day}$). It is found that for a bone-implant interface model of a fixed initial length (250 μm), the rates at which CO and DO occur do not only influence the time needed to close the gap (day 63 at CO: 2 $\mu\text{m/day}$ and day 84 at CO: 1 $\mu\text{m/day}$), but also affect the slope of bone stiffening during the healing process, illustrating the purely kinetic nature of the problem, setting aside chemical or biological reactions.

4. Discussion

This work develops a numerical tool to easily investigate the mechanical properties of the bone-implant interface, as a function of increasing mineral content (or mineral fraction volume) in the overlap regions of mineralized collagen fibril (MCF) networks and the interaction between MCFs. The model described in this work is limited to gap healing in relation to a screw-shaped implant, where primary stability is provided by the threaded design, and is rather general in terms of input parameters, and therefore can be easily modified and/or adapted to include any experimental/physical evidence. In principle, various factors including implant design (geometry and surface features), bulk material, host bone quality, and surgical protocol will influence the kinetics of healing, hence the rates at which distance osteogenesis (DO) and contact osteogenesis (CO) occur.

Taking inspiration from the modeling approach of Wang and Ural [33], our model bridges length scales ranging from the micron scale to the macroscopic structure of the bone-implant interface. As the first step of model development, we elaborate a representative unit cell with homogenized mechanical properties that depend largely on the local mineral content (or mineral volume fraction) and to a lesser extent on the interaction between mineralized collagen fibrils as a function of their geometry and overlap. Next, this representative unit cell is multiplied (extended) to construct a typical, macroscopic bone-implant interface with graded properties that are modulated according to the biological information at hand.

Each MCF unit cell is assumed to behave as a linear elastic isotropic material. One would therefore expect the overall outcome of the model to be linear as well, but this is not the case. Even though the material behavior is linear, it is important to note that the observed nonlinearity of the homogenized Young's modulus is structural in essence, attributable to the kinetics of the CO and DO. More precisely, one can observe the presence of two stages: (i) until gap closure and (ii) stiffening evolution after gap closure. Up to gap closure, the volume of mineralized bone increases, and at the end of this term, the gap between DO and CO fronts is fully closed, and from thereon, the bone continues to gain stiffness gradually. Those two stages reflect clearly in the macroscopic modulus of elasticity of the bone-implant interface model that increases modestly until gap closure followed by a significant increase beyond that point. The obtained E values are not only in agreement with reduced elastic modulus (E_r) values reported for osteonal bone ($\sim 22\text{--}26$ GPa) [47] but also in agreement with E_r values (8.39 ± 0.78 GPa) of bone at a distance of 15–150 μm from the implant surface after one month of healing [48]. Indentation based measurements of elastic modulus, however, are sensitive to the underlying MCF orientation, where E_r values obtained perpendicular and parallel to the collagen fibril axis vary from ~ 11 GPa and ~ 24 GPa, respectively [49].

It is interesting to note that the evolution of the macroscopic interfacial stiffness is reminiscent of well-known physical phenomena such as phase transition, based on volume fractions of compliant/stiff cells, or percolation involving cluster connectivity. For phase transition, one would expect the weak-to-strong transition to be more gradual, based on some sort of (linear) rule of mix-

tures of each phase. Since the transition is not gradual, we will retain here the percolation hypothesis, a graphical illustration of which can be found elsewhere [50]. While we did not perform a mathematical evaluation of the percolation phenomenon, physical insight can be gained from the distributions of the compliant and stiff MCF unit cells. At day 0, the scene is dominated by compliant MCF unit cells that may be assumed to be interconnected as in any random network. As time elapses until gap closure, those compliant unit cells diminish in number, leading to an assumed state of disconnection close to the percolation threshold. As time elapses, stiffer cells appear in increasing numbers and form a strong connected network. This gradual substitution of compliant unit cells by stiffer unit cells and their spatial distribution are deemed to be the responsible factors for the observed percolation.

The present approach allows tracking, seamlessly, each cubic micrometer of bone throughout the process of peri-implant osteogenesis, the heterogeneous distribution of the mechanical properties and the evolution thereof spatially within the bone-implant interface region and over time. While bone turnover has not been addressed in the current work, bone remodeling approaches based on strain for example, as exemplified by Wolff's law and alike [51] can be easily incorporated. Importantly, the strains experienced by bone (in the 30–700 $\mu\epsilon$ range) are not sufficiently high to induce a significant anabolic effect [52], however, it is important to note that a tensile stress of only 1 MPa is being applied. Moreover, we have not included damage evolution deliberately in order to keep the number of parameters to a minimum, but such an addition is definitely compatible with the approach adopted here. The findings reported here concern the mechanical stiffness of the bone-implant interface, and as such, they are independent of the geometrical dimensions of the current model but depend on the bone healing kinetics that were assumed.

Finally, from a clinical perspective, the present results are relevant for the clinical dental community in two aspects. The first relates to the submerged (unloaded) initial healing time that should elapse before a dental implant, for instance, can be safely loaded, an issue that is still under intense debate. Within the limiting assumptions of the model, it appears that the minimum amount of time lapse is precisely that required for gap closure between CO and DO fronts. Next, noting that the present characterization of the interface can be used to model any kind of interface/load combination in a bone-dental implant system, one can now tackle implant stability issues, both primary and secondary, as a reflection of the interfacial physical and mechanical condition over time with the resulting implant micromovements.

A key challenge that remains is to accurately model the rate of bone mineralization, which occurs as distinct phases of primary and secondary mineralization [53]. It is known that certain characteristics of the mineral phase, such as composition (Mg content and Ca/P ratio), crystallinity, and particle size at sites of de novo bone formation differ substantially from the mineral at remodeling sites [54]. Moreover, remodeling events produce distinct structures called 'cement lines' that sharply deviate from adjacent lamellar/osteonal bone in terms of mineral density [55]. Bone remodeling occurs through a combination of load-driven (to adapt the structure to external forces) and non-mechanical (to maintain calcium homeostasis) stimuli [56]. A strong inverse relationship has been described between the frequency of loading and the strain magnitude to induce bone formation or bone resorption, where a loading regime of 100 cycles per day of $\sim 1,000$ $\mu\epsilon$ is sufficient for bone maintenance and higher strains are anabolic [57]. Interestingly, mechanical stimulation has a strong influence on reducing peri-implant bone resorption, but only a limited effect on bone formation [58].

Such characteristics will need to be taken into consideration in the present modeling approach in order to more accurately incor-

porate the impact of renewal, repair, and functional adaption of peri-implant bone. In other words, introduction of eventual remodeling of peri-implant bone may be less straightforward than voids of near-negligible Young's modulus, several tens of micrometers in size, to appear after a given healing duration and subsequently fill with unit cells of mineralized collagen fibrils that progressively increase in mineral density. Host bone quality, for example if the implant is placed in osteoporotic, osteopetrotic, or otherwise healthy bone, can be expected to influence the mechanical behaviour of the interface zone, in particular by the timing and extent of bone remodeling and/or functional adaptation.

5. Conclusion

- We propose here a relatively simple spatio-temporal mechanical model, bridging the MCF unit cell and a macroscopic bone-implant interface.
- The linear elastic stochastic finite element model reveals a highly nonlinear temporal evolution of the interfacial stiffness, with two distinct periods: gap closure and gap stiffening.
- Prior to complete closure of the gap between the two peri-implant bone formation fronts (i.e., CO and DO), the interface possesses a small stiffness that, following gap closure and subsequent stiffening, evolves into a much higher stiffness.
- This stiffness transition is reminiscent of a percolation transition whose threshold corresponds to gap closure.
- The reported observations characterize the various kinetics of CO/DO evolutions that only dictate the time needed for gap closure.
- Potential directions for further development of the model include experimental validation of the model, modification and optimization of the current modeling approach based on quantitative experimental data, and introduction of implant surface roughness and the impact thereof on the biomechanical integrity of the spatio-temporally evolving bone-implant interface.

Declaration of Competing Interest

The authors declare they have no conflict of interest whatsoever

Acknowledgments

This work was supported by the Swedish Foundation for International Cooperation in Research and Higher Education (grant no. [STINT IB2019-8243](#)). J.X. acknowledges the support of Beijing Institute of Technology (Research Fund Program for Young Scholars). A.P. acknowledges the financial support from the Swedish Research Council (grant no. [2020-04715](#)). F.A.S. was supported by the Svenska Sällskapet för Medicinsk Forskning (SSMF) postdoctoral scholarship. The authors wish to thank the three anonymous reviewers for their many valuable suggestions that helped improving the manuscript.

References

- [1] R. Adell, B. Eriksson, U. Lekholm, P.I. Brånemark, T. Jemt, Long-term follow-up study of osseointegrated implants in the treatment of totally edentulous jaws, *Int. J. Oral Maxillofac. Implants.* 5 (1990) 347–359.
- [2] M.S. Howe, W. Keys, D. Richards, Long-term (10-year) dental implant survival: a systematic review and sensitivity meta-analysis, *J. Dent.* (2019), doi:[10.1016/j.jdent.2019.03.008](#).
- [3] J. Lindhe, N.P. Lang, T. Berglundh, W.V. Giannobile, M. Sanz, *Clinical periodontology and implant dentistry*, 6th ed., Wiley Blackwell, 2015.
- [4] F.A. Shah, P. Thomsen, A. Palmquist, Osseointegration and current interpretations of the bone-implant interface, *Acta Biomater* 84 (2019) 1–15, doi:[10.1016/j.actbio.2018.11.018](#).
- [5] T. Albrektsson, P.-I. Brånemark, H.-A. Hansson, J. Lindström, Osseointegrated titanium implants: requirements for ensuring a long-lasting, direct bone-to-implant anchorage in man, *Acta Orthop. Scand.* 52 (1981) 155–170, doi:[10.3109/17453678108991776](#).
- [6] A. Palmquist, A multiscale analytical approach to evaluate osseointegration, *J. Mater. Sci. Mater. Med.* 29 (2018) 60, doi:[10.1007/s10856-018-6068-y](#).
- [7] D.A. Puleo, A. Nanci, Understanding and controlling the bone-implant interface, *Biomaterials* 20 (1999) 2311–2321, doi:[10.1016/S0142-9612\(99\)00160-X](#).
- [8] J.E. Davies, Bone bonding at natural and biomaterial surfaces, *Biomaterials* 28 (2007) 5058–5067, doi:[10.1016/j.biomaterials.2007.07.049](#).
- [9] Y. Shibata, Y. Tanimoto, N. Maruyama, M. Nagakura, A review of improved fixation methods for dental implants. part II: biomechanical integrity at bone-implant interface, *J. Prosthodont. Res.* (2015), doi:[10.1016/j.jpor.2015.01.003](#).
- [10] V. Sansalone, S. Naili, V. Bousson, C. Bergot, F. Peyrin, J. Zarka, J.D. Laredo, G. Haïat, Determination of the heterogeneous anisotropic elastic properties of human femoral bone: from nanoscopic to organ scale, *J. Biomech.* 43 (2010) 1857–1863, doi:[10.1016/j.jbiomech.2010.03.034](#).
- [11] L. Podshivalov, A. Fischer, P.Z. Bar-Yoseph, 3D hierarchical geometric modeling and multiscale FE analysis as a base for individualized medical diagnosis of bone structure, *Bone* 48 (2011) 693–703, doi:[10.1016/j.bone.2010.12.022](#).
- [12] L. Podshivalov, A. Fischer, P.Z. Bar-Yoseph, On the road to personalized medicine: multiscale computational modeling of bone tissue, *Arch. Comput. Methods Eng.* 21 (2014) 399–479, doi:[10.1007/s11831-014-9120-1](#).
- [13] R. Korabi, K. Shemtov-Yona, A. Dorogoy, D. Rittel, The failure envelope concept applied to the bone-dental implant system, *Sci. Rep.* 7 (2017) 2051, doi:[10.1038/s41598-017-02282-2](#).
- [14] D. Rittel, A. Dorogoy, K. Shemtov-Yona, Modeling the effect of osseointegration on dental implant pullout and torque removal tests, *Clin. Implant Dent. Relat. Res.* (2018), doi:[10.1111/cid.12645](#).
- [15] G. Haïat, X. Gao, M. Fraulob, Biomechanical behaviours of the bone-implant interface: a review, (2019). <https://doi.org/10.1098/rsif.2019.0259>.
- [16] A. Eser, K. Akça, S. Eckert, M.C. Çehreli, Nonlinear finite element analysis versus ex vivo strain gauge measurements on immediately loaded implants, *Int. J. Oral Maxillofac. Implant.* (2009).
- [17] M.L. Raffia, V.H. Nguyen, G. Haïat, Micromechanical modeling of the contact stiffness of an osseointegrated bone-implant interface, *Biomed. Eng. Online*, 18 (2019) 1–18, doi:[10.1186/s12938-019-0733-3](#).
- [18] R.M. Wazen, J.A. Currey, H. Guo, J.B. Brunski, J.A. Helms, A. Nanci, Micromotion-induced strain fields influence early stages of repair at bone-implant interfaces, *Acta Biomater* 9 (2013) 6663–6674, doi:[10.1016/j.actbio.2013.01.014](#).
- [19] N. Reznikov, R. Shahar, S. Weiner, Bone hierarchical structure in three dimensions, *Acta Biomater* 10 (2014) 3815–3826, doi:[10.1016/j.actbio.2014.05.024](#).
- [20] F.A. Shah, Magnesium whitlockite – omnipresent in pathological mineralisation of soft tissues but not a significant inorganic constituent of bone, *Acta Biomater* (2021), doi:[10.1016/j.actbio.2021.02.021](#).
- [21] B. Alexander, T.L. Daulton, G.M. Genin, J. Lipner, J.D. Pasteris, B. Wopenka, S. Thomopoulos, The nanometre-scale physiology of bone: steric modelling and scanning transmission electron microscopy of collagen-mineral structure, *J. R. Soc. Interface*, 9 (2012) 1774–1786, doi:[10.1098/rsif.2011.0880](#).
- [22] B. Depalle, Z. Qin, S.J. Shefelbine, M.J. Buehler, Large deformation mechanisms, plasticity, and failure of an individual collagen fibril with different mineral content, *J. Bone Miner. Res.* 31 (2016) 380–390, doi:[10.1002/jbmr.2705](#).
- [23] O.A. Tertuliano, J.R. Greer, The nanocomposite nature of bone drives its strength and damage resistance, *Nat. Mater.* 15 (2016) 1195–1202, doi:[10.1038/nmat4719](#).
- [24] A. Dorogoy, D. Rittel, K. Shemtov-Yona, R. Korabi, Modeling dental implant insertion, *J. Mech. Behav. Biomed. Mater.* 68 (2017) 42–50, doi:[10.1016/j.jmbmb.2017.01.021](#).
- [25] F.A. Shah, B. Nilsson, R. Brånemark, P. Thomsen, A. Palmquist, The bone-implant interface – nanoscale analysis of clinically retrieved dental implants, *Nanomedicine Nanotechnology, Biol. Med.* 10 (2014) 1729–1737, doi:[10.1016/j.nano.2014.05.015](#).
- [26] G. Sundell, C. Dahlin, M. Andersson, M. Thuvander, The bone-implant interface of dental implants in humans on the atomic scale, *Acta Biomater* 48 (2017) 445–450, doi:[10.1016/j.actbio.2016.11.044](#).
- [27] K. Grandfield, S. Gustafsson, A. Palmquist, Where bone meets implant: the characterization of nano-osseointegration, *Nanoscale* 5 (2013) 4302–4308, doi:[10.1039/c3nr00826f](#).
- [28] S. Le Cann, E. Törnquist, I. Silva Barreto, M. Fraulob, H. Albin Lomami, M. Verezhak, M. Guizar-Sicairos, H. Isaksson, G. Haïat, Spatio-temporal evolution of hydroxyapatite crystal thickness at the bone-implant interface, *Acta Biomater.* 116 (2020) 391–399, doi:[10.1016/j.actbio.2020.09.021](#).
- [29] F.A. Shah, X. Wang, P. Thomsen, K. Grandfield, A. Palmquist, High-resolution visualization of the osteocyte lacuno-canalicular network juxtaposed to the surface of nanotextured titanium implants in human, *ACS Biomater. Sci. Eng.* 1 (2015) 305–313, doi:[10.1021/ab500127y](#).
- [30] F.A. Shah, P. Stenlund, A. Martinelli, P. Thomsen, A. Palmquist, Direct communication between osteocytes and acid-etched titanium implants with a sub-micron topography, *J. Mater. Sci. Mater. Med.* 27 (2016) 1–9, doi:[10.1007/s10856-016-5779-1](#).
- [31] M. Büniger, M. Foss, K. Erlacher, H. Li, X. Zou, B. Langdahl, C. Büniger, H. Birkedal, F. Besenbacher, J. Pedersen, Bone nanostructure near titanium and porous tantalum implants studied by scanning small angle x-ray scattering, *Eur. Cells Mater.* 12 (2006) 81–91, doi:[10.22203/eCm.v012a10](#).

- [32] Y. Wang, A. Ural, Mineralized collagen fibril network spatial arrangement influences cortical bone fracture behavior, *J. Biomech.* 66 (2018) 70–77, doi:[10.1016/j.jbiomech.2017.10.038](https://doi.org/10.1016/j.jbiomech.2017.10.038).
- [33] Y. Wang, A. Ural, A finite element study evaluating the influence of mineralization distribution and content on the tensile mechanical response of mineralized collagen fibril networks, *J. Mech. Behav. Biomed. Mater.* (2019), doi:[10.1016/j.jmbbm.2019.07.019](https://doi.org/10.1016/j.jmbbm.2019.07.019).
- [34] Y. Wang, A. Ural, Effect of modifications in mineralized collagen fibril and extra-fibrillar matrix material properties on submicroscale mechanical behavior of cortical bone, *J. Mech. Behav. Biomed. Mater.* 82 (2018) 18–26, doi:[10.1016/j.jmbbm.2018.03.013](https://doi.org/10.1016/j.jmbbm.2018.03.013).
- [35] J.E. Davies, Understanding Peri-Implant Endosseous Healing, *J. Dent. Educ.* 67 (2003) 932–949, doi:[10.1002/j.0022-0337.2003.67.8.tb03681.x](https://doi.org/10.1002/j.0022-0337.2003.67.8.tb03681.x).
- [36] D.D. Bosshardt, V. Chappuis, D. Buser, Osseointegration of titanium, titanium alloy and zirconia dental implants: current knowledge and open questions, *Periodontol* 73 (2017) (2000) 22–40, doi:[10.1111/prd.12179](https://doi.org/10.1111/prd.12179).
- [37] A.W. Eberhardt, A. Yeager-Jones, H.C. Blair, Regional trabecular bone matrix degeneration and osteocyte death in femora of glucocorticoid-treated rabbits, *Endocrinology* 142 (2001) 1333–1340, doi:[10.1210/endo.142.3.8048](https://doi.org/10.1210/endo.142.3.8048).
- [38] S.J. Jones, A. Boyde, J.B. Pawley, Osteoblasts and collagen orientation, *Cell Tissue Res.* 159 (1975) 73–80, doi:[10.1007/BF00231996](https://doi.org/10.1007/BF00231996).
- [39] F.A. Shah, E. Zanghellini, A. Matic, P. Thomsen, A. Palmquist, The orientation of nanoscale apatite platelets in relation to osteoblastic-osteocyte lacunae on trabecular bone surface, *Calcif. Tissue Int.* 98 (2016) 193–205, doi:[10.1007/s00223-015-0072-8](https://doi.org/10.1007/s00223-015-0072-8).
- [40] D.R. Carter, W.C. Hayes, Bone compressive strength: the influence of density and strain rate, *Science* (80-) 194 (1976) 1174–1176 <http://www.sciencemag.org/content/194/4270/1174.short>.
- [41] Z. Yosibash, R. Padan, L. Joskowicz, C. Milgrom, A CT-based high-order finite element analysis of the human proximal femur compared to in-vitro experiments, *J. Biomech. Eng.* 129 (2007) 297–309, doi:[10.1115/1.2720906](https://doi.org/10.1115/1.2720906).
- [42] J.Y. Rho, T.Y. Tsui, G.M. Pharr, Elastic properties of human cortical and trabecular lamellar bone measured by nanoindentation, *Biomaterials* 18 (1997) 1325–1330, doi:[10.1016/S0142-9612\(97\)00073-2](https://doi.org/10.1016/S0142-9612(97)00073-2).
- [43] ABAQUS, Simulia, Abaqus/CAE Version 6.14-2. (2014).
- [44] A.J.C. Ladd, J.H. Kinney, Numerical errors and uncertainties in finite-element modeling of trabecular bone, *J. Biomech.* 31 (1998) 941–945, doi:[10.1016/S0021-9290\(98\)00108-0](https://doi.org/10.1016/S0021-9290(98)00108-0).
- [45] D.D. Cody, G.J. Gross, F.J. Hou, H.J. Spencer, S.A. Goldstein, D.P. Fyhrie, Predicted by finite element models than QCT and DXA, *J. Biomech.* 32 (1999) 1013–1020.
- [46] C. Ruff, B. Holt, E. Trinkaus, Who's afraid of the big bad Wolff?: "Wolff's law" and bone functional adaptation, *Am. J. Phys. Anthropol.* 129 (2006) 484–498, doi:[10.1002/ajpa.20371](https://doi.org/10.1002/ajpa.20371).
- [47] H.S. Gupta, U. Stachewicz, W. Wagermaier, P. Roschger, H.D. Wagner, P. Fratzl, Mechanical modulation at the lamellar level in osteonal bone, *J. Mater. Res.* 21 (2006) 1913–1921, doi:[10.1557/jmr.2006.0234](https://doi.org/10.1557/jmr.2006.0234).
- [48] M.C. Chang, C.C. Ko, C.C. Liu, W.H. Douglas, R. DeLong, W.J. Seong, J. Hodges, K.N. An, Elasticity of alveolar bone near dental implant-bone interfaces after one month's healing, *J. Biomech.* 36 (2003) 1209–1214, doi:[10.1016/S0021-9290\(03\)00113-1](https://doi.org/10.1016/S0021-9290(03)00113-1).
- [49] P. Fratzl, H.S. Gupta, E.P. Paschalis, P. Roschger, Structure and mechanical quality of the collagen-mineral nano-composite in bone, *J. Mater. Chem.* 14 (2004) 2115–2123, doi:[10.1039/b402005g](https://doi.org/10.1039/b402005g).
- [50] C. DeArmitt, Applied Plastics Engineering Handbook, in: M. Kutz (Ed.), Appl. Plast. Eng. Handb., Elsevier, 2011, p. 461, doi:[10.1016/C2010-0-67336-6](https://doi.org/10.1016/C2010-0-67336-6).
- [51] H.M. Frost, Bone's mechanostat: A 2003 update, *Anat. Rec.* 275A (2003) 1081–1101, doi:[10.1002/ar.a.10119](https://doi.org/10.1002/ar.a.10119).
- [52] J.W.C. Dunlop, M.A. Hartmann, Y.J. Bréchet, P. Fratzl, R. Weinkamer, New suggestions for the mechanical control of bone remodeling, *Calcif. Tissue Int.* 85 (2009) 45–54, doi:[10.1007/s00223-009-9242-x](https://doi.org/10.1007/s00223-009-9242-x).
- [53] S.V. Komarova, L. Safranek, J. Gopalakrishnan, M. jung Y. Ou, M.D. McKee, M. Murshed, F. Rauch, E. Zuhre, Mathematical model for bone mineralization, *Front. Cell Dev. Biol.* 3 (2015) 1–11, doi:[10.3389/fcell.2015.00051](https://doi.org/10.3389/fcell.2015.00051).
- [54] A. Roschger, W. Wagermaier, S. Gamsjaeger, N. Hassler, I. Schmidt, S. Blouin, A. Berzlanovich, G.M. Gruber, R. Weinkamer, P. Roschger, E.P. Paschalis, K. Klaushofer, P. Fratzl, Newly formed and remodeled human bone exhibits differences in the mineralization process, *Acta Biomater.* 104 (2020) 221–230, doi:[10.1016/j.actbio.2020.01.004](https://doi.org/10.1016/j.actbio.2020.01.004).
- [55] P. Milovanovic, A. vom Scheidt, K. Mletzko, G. Sarau, K. Püschel, M. Djuric, M. Amling, S. Christiansen, B. Busse, Bone tissue aging affects mineralization of cement lines, *Bone* 110 (2018) 187–193, doi:[10.1016/j.bone.2018.02.004](https://doi.org/10.1016/j.bone.2018.02.004).
- [56] P. Christen, K. Ito, R. Ellouz, S. Boutroy, E. Sornay-Rendu, R.D. Chapurlat, B. Van Rietbergen, Bone remodelling in humans is load-driven but not lazy, *Nat. Commun.* 5 (2014), doi:[10.1038/ncomms5855](https://doi.org/10.1038/ncomms5855).
- [57] E. Ozcivici, Y.K. Luu, B. Adler, Y.X. Qin, J. Rubin, S. Judex, C.T. Rubin, Mechanical signals as anabolic agents in bone, *Nat. Rev. Rheumatol.* 6 (2010) 50–59, doi:[10.1038/nrrheum.2009.239](https://doi.org/10.1038/nrrheum.2009.239).
- [58] Z. Li, D. Betts, G. Kuhn, M. Schirmer, R. Müller, D. Ruffoni, Mechanical regulation of bone formation and resorption around implants in a mouse model of osteopenic bone, *J. R. Soc. Interface.* 16 (2019), doi:[10.1098/rsif.2018.0667](https://doi.org/10.1098/rsif.2018.0667).